

# The formation of CDM haloes II: collapse time and tides

Mikolaj Borzyszkowski\*, Aaron D. Ludlow and Cristiano Porciani

*Argelander-Institut für Astronomie, Auf dem Hügel 71, D-53121 Bonn, Germany*

1 March 2022

## ABSTRACT

We use two cosmological simulations of structure formation in the  $\Lambda$ CDM scenario to study the evolutionary histories of dark-matter haloes and to characterize the Lagrangian regions from which they form. We focus on haloes identified at redshift  $z_{\text{id}} = 0$  and show that the classic ellipsoidal collapse model systematically overestimates their collapse times. If one imposes that halo collapse takes place at  $z_{\text{id}}$ , this model requires starting from a significantly lower linear density contrast than what is measured in the simulations at the locations of halo formation. We attempt to explain this discrepancy by testing two key assumptions of the model. First, we show that the tides felt by collapsing haloes due to the surrounding large-scale structure evolve non-linearly. Although this effect becomes increasingly important for low-mass haloes, accounting for it in the ellipsoidal collapse model only marginally improves the agreement with N-body simulations. Second, we track the time evolution of the physical volume occupied by forming haloes and show that, after turnaround, it generally stabilizes at a well-defined redshift,  $z_c > z_{\text{id}}$ , contrary to the basic assumption of extended Press-Schechter theory based on excursion sets. We discuss the implications of this result for understanding the origin of the mass-dependence and scatter in the linear threshold for halo formation. Finally, we show that, when tuned for collapse at  $z_c$ , a modified version of the ellipsoidal collapse model that also accounts for the triaxial nature of protohaloes predicts their linear density contrast in an unbiased way.

**Key words:** cosmology: theory – dark matter – galaxies: haloes

## 1 INTRODUCTION

The formation of dark-matter haloes through gravitational instability of small density perturbations is a formidable non-linear problem. Most of our current understanding of the process is based on N-body simulations, yet valuable theoretical insight can be gained through analytic models that attempt to approximate the growth of structure.

Most theoretical models are based on the assumption that haloes of mass  $M$  originate from compact Lagrangian patches of initial comoving size  $R \propto M^{1/3}$  in which conditions are favorable for collapse. In the most simplistic picture, the collapse process can be approximated by following the evolution of a spherically symmetric perturbation with a top-hat density profile and vanishing initial peculiar velocities in a otherwise homogeneous and expanding background (Partridge & Peebles 1967; Peebles 1967; Gunn & Gott 1972; Peebles 1980). In this “spherical collapse model”, perturbations that are dense enough to form bound structures decouple from the background expansion, eventually reverse their motion and start collapsing at an increasingly faster rate. The mathematical solution of the equation

of motion leads to a singularity, but the development of non-radial motions due to the imperfect symmetry of any realistic perturbation is expected to halt the collapse and form a stable structure in virial equilibrium. Energy conservation suggests that the final radius of the bound structure should be approximately one half of the maximum “turn-around” radius (Gott & Rees 1975), or smaller in the presence of a cosmological constant (Lahav et al. 1991).

Based on the statistical properties of Gaussian random fields, Press & Schechter (1974) developed a model for the number density of dark-matter haloes as a function of their mass and redshift. The model assumes that all Lagrangian patches in which the linearly extrapolated density contrast at redshift  $z$  lies above a critical value  $\delta_c$  (of order unity) have collapsed to form bound haloes by that redshift. For practical applications, one has to choose a specific value for  $\delta_c$  that matches a given halo definition. In an Einstein-de Sitter universe, spherical collapse produces virialized haloes with a final mean overdensity of  $\Delta_{\text{vir}} = 18\pi^2 \simeq 178$  which occurs when the linear density contrast is  $\delta_c = (3/5)(3\pi/2)^{2/3} \simeq 1.686$  (Kaiser 1984; Bardeen et al. 1986; Efstathiou et al. 1988). For different cosmological models, these quantities acquire a red-

\* E-mail: mikolajb@astro.uni-bonn.de

shift dependence which, however, is very weak for  $\delta_c$  (e.g. Eke, Cole & Frenk 1996).

Bond et al. (1991) provided a sounder theoretical basis for the Press-Schechter mass function using the theory of “excursion-sets”. A key assumption of their model is that a halo identified at redshift  $z_{\text{id}}$  should form by collecting all matter initially contained within the largest possible region over which the mean linear overdensity is  $\delta_L(z_{\text{id}}) = \delta_c$ . In other words, the Lagrangian boundary of a halo coincides with the outermost shell which is collapsing at redshift  $z_{\text{id}}$ . However, for  $\delta_c \simeq 1.686$ , this method yields halo mass functions that agree only qualitatively with those extracted from N-body simulations; they exhibit systematic shifts from the numerical result at both low and high masses which can be eliminated by adopting an effective mass-dependent threshold for halo formation  $\delta_c(M)$  (e.g. Sheth & Tormen 1999).

One possible explanation for this discrepancy is that the spherical collapse model is too simplistic. For example, N-body simulations have shown that dark-matter haloes originate from elongated Lagrangian regions whose longest geometric axis aligns with the direction of maximum gravitational compression (Porciani, Dekel & Hoffman (2002), see also Despali, Tormen & Sheth (2013); Lee & Pen (2000); Ludlow, Borzyszkowski & Porciani (2014), hereafter Paper I) The collapse of an ellipsoidal top-hat overdensity amplifies any initial departure from sphericity whether perturbations are isolated (Lynden-Bell 1964; Lin, Mestel & Shu 1965) or embedded in a uniform and expanding background (Icke 1973; White & Silk 1979; Peebles 1980). The presence of external tides generated by large-scale structure, however, is expected to influence the dynamics of collapsing ellipsoids (e.g. Hoffman 1986; Bertschinger & Jain 1994). These tides were incorporated into the EC model by Eisenstein & Loeb (1995) and Bond & Myers (1996, hereafter BM96) in a way that recovers the Zel’dovich approximation (Zel’dovich 1970) in the linear regime. In the latter formulation, an initially spherical overdensity is sheared into a collapsing ellipsoid by the action of external tides. The perturbation first reaches zero extension along the direction of largest compression, at which point orbit crossing occurs and the single-stream fluid equations cease to be valid. This can be prevented, however, by artificially halting collapse once the axis has shrunk by a critical factor  $(18\pi^2)^{-1/3} \simeq 0.178$  with respect to the background expansion (BM96; Angrick & Bartelmann (2010)).

Using this model, and defining the collapse time of a perturbation to be the epoch at which its last principal axis freezes out, Sheth, Mo & Tormen (2001) showed that more strongly sheared perturbations require higher initial density contrasts to overcome the tidal stretching and collapse by a particular time. Approximating the locations of halo formation as random points in a Gaussian random field, this “ellipsoidal-collapse threshold”,  $\delta_{\text{ec}}$ , can be expressed in terms of the rms amplitude of linear density perturbations,  $\sigma(M)$ , or equivalently in terms of halo mass. The value of  $\delta_{\text{ec}}$  typically increases towards lower masses in a way that resembles the measured mean linear overdensities of dark-matter “protohaloes” identified in the initial conditions of N-body simulations (Robertson et al. (2009); Elia, Ludlow & Porciani (2012); Paper I); this is generally interpreted as a reflection of the stronger tides felt, on average, by less massive haloes.

Sheth, Mo & Tormen (2001) used the ellipsoidal-collapse threshold to predict the mass function and bias of dark-matter haloes in the excursion-set formalism. If  $\delta_{\text{ec}}$  is rescaled by an ad-hoc factor, this solution offers better agreement with the results of numerical simulations than calculations based on the spherical collapse model. Sheth, Mo & Tormen (2001) justified the rescaling by noting that the halo finder that was used in the simulations did not necessarily match the final overdensity of the haloes produced by the EC model.

The EC model of BM96, however, cannot account for the considerable scatter in the measured linear overdensities,  $\delta_L$ , of regions that later collapse to form haloes of a particular mass  $M$ , and additionally fails to explain why  $\delta_L$  depends strongly on the characteristic half-mass formation time of the halo (Paper I). In that companion paper we showed that, although the average overdensity of dark-matter protohaloes tends to scale with external tides as described by the ellipsoidal model of BM96, the majority of recently collapsed haloes fall systematically *below* the model-predicted threshold for collapse. Hahn & Paranjape (2014) reached similar conclusions using warm-dark-matter simulations and thus provided further evidence that the ellipsoidal model systematically over-predicts the collapse time of a perturbation.

These puzzling results can be explained by a modified EC model that allows for initial asymmetry in the shape of the linear perturbations. Changing the initial axis lengths alters their individual collapse times and therefore modulates the initial density contrast required for complete collapse by a particular redshift. In Paper I, we showed that a model tuned to match the Lagrangian shapes of dark-matter protohaloes in numerical simulations can accurately reproduce their linear overdensities as well as its dependence on the initial departure from sphericity. A nice feature of this model is that the three principal axes of the perturbation freeze out almost simultaneously, similar to the case of spherical collapse. There is one caveat, however: the predicted threshold for collapse at redshift  $z_{\text{id}}$  only traces the overdensities of recently collapsed haloes for a given external tidal field and lies below the mean value measured for fixed halo mass and identification redshift. This begs the question of why dark-matter protohaloes with linear overdensities substantially above the ellipsoidal-collapse threshold exist at all, when virtually none with lower initial densities are found in cosmological simulations. We address these questions here using different versions of the ellipsoidal collapse model combined with the same numerical simulations (and dark-matter halo catalogs) as in Paper I. We anticipate that our findings imply a major revision of the standard lore for halo formation and raise questions regarding the validity of the excursion-set ansatz.

This paper is structured as follows. The dynamical model for ellipsoidal collapse is presented in Section 2, while our simulations, halo catalogs and analysis techniques are discussed in Section 3. Our main results are presented in Section 4, with a discussion of the implications of our results in Section 5. The conclusions are then summarized in Section 6.

## 2 THE ELLIPSOIDAL COLLAPSE MODEL

The dynamical equations for the collapse of a constant density ellipsoid in the presence of an external tidal field were derived in Paper I. We assume that the principal axes of the perturbation are aligned with the eigenvectors of the external tidal field (Porciani, Dekel & Hoffman 2002), and that the background expansion is driven by a pressureless matter density and a cosmological constant (see Del Popolo (2002) for a similar model).

In a Cartesian coordinate system that is aligned with the principal frame of the ellipsoid, the differential equation for the axis lengths,  $r_i$ , is (BM96)

$$\frac{\ddot{r}_i}{r_i} = \Omega_\Lambda H_0^2 - \frac{3}{2} \frac{\Omega_M H_0^2}{a^3} \left( \frac{1}{3} + \lambda_i^{\text{tot}} \right), \quad (1)$$

where the dots denote time derivatives;  $H_0$  is the Hubble constant;  $a$  the expansion factor; and  $\Omega_M$  and  $\Omega_\Lambda$  are the present-day densities of matter and the cosmological constant,  $\Lambda$ , normalized to the critical density,  $\rho_{\text{crit}} = 3H_0^2/8\pi G$ , where  $G$  is Newton's gravitational constant. The tidal field,  $\lambda_i^{\text{tot}}$ , is given by

$$\lambda_i^{\text{tot}} = \lambda_i^{\text{ext}} + \frac{\delta}{3} + \frac{\beta_i \delta}{2}, \quad (2)$$

where  $\delta = \delta(a)$  is the time-dependent density contrast of the ellipsoid. Note that eq. (2) contains contributions from both external tides,  $\lambda_i^{\text{ext}}$ , as well as an internal component generated by the ellipsoid itself. The latter can be calculated explicitly using elliptic integrals:

$$\beta_i = r_1 r_2 r_3 \int_0^\infty \frac{d\tau}{(\tau + r_i^2) \prod_{k=1}^3 \sqrt{\tau + r_k^2}} - \frac{2}{3}, \quad (3)$$

where the  $2/3$  guarantees  $\sum_i \beta_i = 0$ . Note that for a spherical geometry, the integral in eq. (3) is equal to  $2/3$  and internal tides vanish. Initial condition for eq. (1) are set at some early time,  $a_0$ , using the Zel'dovich approximation.

The external tidal field,  $\lambda_i^{\text{ext}}$ , however, as well as its time evolution, must be explicitly specified. One common assumption is that  $\lambda_i^{\text{ext}}$  is generated by structure on large scales and evolves from its initial value according to linear theory; another possibility is that  $\lambda_i^{\text{ext}}$  is dominated by the (non-linear) tidal field generated by the perturbation itself (BM96). A model which interpolates between these two regimes was recently proposed by Angrick & Bartelmann (2010). In this approach, one adopts the non-linear model  $\lambda_i^{\text{ext}}(t)$  until axis  $i$  turns around, at which point its corresponding eigenvalue continues to evolve linearly. In our model we will initially assume that external tides are generated by large-scale structure and grow with time according to the linear growth factor,  $D(z)$ ; internal tides are calculated self-consistently using the time-dependent shape of the ellipsoid. In Section 4.2 we will revisit the issue of external tides in more detail, in order to test the assumption made above regarding their time evolution.

The collapse and virialization of the perturbation is generally approximated in this model by freezing the individual axes when they reach a size  $r_{f,i} = f q_i a$  (BM96). Here  $q_i$  is the *initial* comoving length of axis  $i$ , and the parameter  $f$  is usually set to 0.178. In the case of spherical collapse in an Einstein-de Sitter universe, this choice ensures that the perturbation has a density contrast of  $\delta \approx 178$  at the moment of collapse. Note, however, that a particular choice of  $f$  has

no fundamental physical motivation and may depend on the nature of collapse (e.g., whether spherical or ellipsoidal) or on the background cosmological model. A more general virialization condition based on the tensor virial theorem was suggested by Angrick & Bartelmann (2010). However, since the late stages of collapse generally occur quite rapidly, such modifications have only a minor effect on axis collapse times, from which density thresholds are inferred. For the sake of simplicity, and to ease comparison with previous work, we adopt the traditional freezing factor  $f = 0.178$  for our EC model as well, but return this point in Section 4.3.

## 3 NUMERICAL METHODS

### 3.1 The Simulations

Our analysis focuses on dark-matter haloes identified at  $z_{\text{id}} = 0$  in two cosmological simulations of structure formation in the standard  $\Lambda$ CDM cosmology. These simulations are the same as those described in Paper I (see also Pillepich, Porciani & Hahn 2010). We therefore summarize here only their main aspects, and refer the reader to that work for further details.

Both runs followed the evolution of the dark-matter component using  $1024^3$  equal mass particles. The periodic boxes have side lengths equal to  $150 h^{-1}$  Mpc and  $1200 h^{-1}$  Mpc. Each run was carried out with a lean version of the simulation code GADGET (Springel, Yoshida & White 2001) and adopted the following cosmological parameters:  $\Omega_M = 0.279$ ,  $\Omega_\Lambda = 1 - \Omega_M = 0.721$ ,  $n_s = 0.96$ ,  $\sigma_8 = 0.817$ , and  $H_0 = 73 \text{ km s}^{-1} \text{ Mpc}^{-1}$ . Here  $n_s$  is the spectral index of primordial density fluctuations;  $\sigma_8$  is the rms density fluctuation measured in  $8 h^{-1}$  Mpc spheres, linearly extrapolated to  $z = 0$ . These values are consistent with the WMAP 5-year data release (Komatsu et al. 2009). The resulting particle masses are  $m_p = 2.43 \times 10^8 h^{-1} M_\odot$  and  $m_p = 1.24 \times 10^{11} h^{-1} M_\odot$  for the  $150 h^{-1}$  Mpc and  $1200 h^{-1}$  Mpc boxes.

Initial conditions for the simulations were produced using the Zel'Dovich approximation for a starting redshift of  $z_{\text{start}} = 70$  and  $50$  for the small and large box, respectively. As discussed in detail by Pillepich, Porciani & Hahn (2010), these choices of  $z_{\text{start}}$  are sufficient to erase all transient artifacts in the halo mass function by  $z = 0$ . During each simulation, 30 snapshots were saved between  $z = 10$  and  $0$  in logarithmically spaced intervals of  $(1+z)^{-1}$ .

### 3.2 Halo Catalogs

We identified dark-matter haloes in each simulation output using a friends-of-friends (FOF) halo finder with a linking length equal to 0.2 times the mean nearest-neighbour distance. All haloes with at least  $N_{\text{FOF}} = 32$  particles were included in the halo catalogs. Once all dark-matter haloes were identified, the formation histories of  $z_{\text{id}} = 0$  haloes were constructed by tracing each halo's most massive progenitor backwards through all previous simulation outputs. Accretion histories defined in this way can be used to provide simple estimates of halo formation times, such as the redshift  $z_{50}$  at which 50 per cent of the halo's final mass had first assembled into one main progenitor.

We will also consider the Lagrangian “protohaloes” of each  $z = 0$  halo, which can be easily identified by tracing all halo particles back to the initial conditions of the simulation. In this paper we will only consider haloes that, at  $z = 0$ , are composed of at least  $N_{\text{FOF}} = 1000$  particles, unless explicitly stated otherwise.

In order to test the sensitivity of our results to the adopted halo definition, we have also built halo catalogs using a spherical overdensity (SO) halo finder. This algorithm grows spheres around local density maxima until they reach a density contrast of  $\Delta$  times the mean matter density. We adopted  $\Delta = 100, 200$  and  $500$ , and repeated all aspects of the analysis using these alternative halo definitions. We will distinguish the characteristics of haloes identified by the FOF or SO algorithms using subscripts. The FOF halo mass, for example, will be denoted  $M_{\text{FOF}}$ , whereas  $M_{200}$  defines the SO mass based on an overdensity of  $\Delta = 200$ . The main results of our work will be presented for the FOF halo definition; the results for SO haloes are summarized in Appendix A.

### 3.3 Analysis Techniques

The EC model described in Section 2 depends explicitly on the initial axis ratios of the collapsing overdensity. Since in practice these are free parameters, we will constrain their values using the shapes of protohaloes identified in the initial conditions of our simulation.

We characterize the shapes of dark-matter haloes and protohaloes using the inertia tensor, defined

$$I_{ij} = m_p \sum_k x_{k,i} x_{k,j}, \quad (4)$$

where  $\mathbf{x}_k$  is the distance vector between particle  $k$  and the halo’s center-of-mass; the  $i$  and  $j$  are the projected lengths of  $\mathbf{x}_k$  along each coordinate direction. This matrix can be diagonalized to obtain the principal axis lengths of the ellipsoid,  $q_1 \geq q_2 \geq q_3$ , which can be used to characterize halo shapes in terms of their ratios:  $q_2/q_1$  and  $q_3/q_1$ , for example, are the intermediate-to-major and minor-to-major axis ratios. The eigenvectors of the inertia tensor define the principal axis frame, and will be denoted  $\hat{\mathbf{i}}_i$ .

As discussed in Paper I, the shapes of protohalo boundaries are closely related to the external tidal field acting upon them. Protohaloes have strongly triaxial shapes whose principal directions align closely with those of the surrounding tides. When estimating the tides acting upon a given protohalo, it is therefore desirable to move beyond simple spherical filtering of the tidal field, and attempt to incorporate additional information on the shape of the protohalo as well.

Here we propose a novel method to estimate the *average* tidal field acting upon a protohalo as it collapses to form a non-linear object. We start by calculating the density contrast field on a  $1024^3$  grid that covers the entire simulation volume. Densities are assigned to each grid element using cloud-in-cell interpolation (Hockney & Eastwood 1988). Within each grid element, we also calculate the tidal deformation tensor,

$$D_{ij} = \frac{\partial^2 \Phi}{\partial x_i \partial x_j}, \quad (5)$$

using standard Fourier techniques. Here  $\Phi$  is the peculiar gravitational potential, which is related to the density contrast by Poisson’s equation:  $\nabla^2 \Phi = \delta$ . This field can be used to compute the total strength and orientation of the tidal field over an arbitrary volume,  $V$  (for example, a protohalo), in the following way. We first compute the magnitude of  $D_{ij}$  along the direction  $\boldsymbol{\eta}$  using

$$\lambda = \sum_V \boldsymbol{\eta} \cdot \mathbf{D} \cdot \boldsymbol{\eta}, \quad (6)$$

where the sum is over all grid cells contained within the volume. We then iteratively determine the orientation of  $\boldsymbol{\eta}$  that minimizes  $\lambda$ ; this defines the direction  $\mathbf{d}_3$  and its magnitude  $\lambda_3$ . In the plane perpendicular to  $\mathbf{d}_3$ , we then search for the direction  $\boldsymbol{\eta} = \mathbf{d}_1$  that maximizes eq. (6), which also determines  $\lambda_1$ . This constrains the direction  $\mathbf{d}_2$  since it is, by definition, perpendicular to both  $\mathbf{d}_1$  and  $\mathbf{d}_3$ ;  $\lambda_2$  is then determined using eq. (6) along the direction  $\boldsymbol{\eta} = \mathbf{d}_2$ . In this way we estimate the total tidal tensor, described by the  $\lambda_i$ s and  $\mathbf{d}_i$ s, acting on the volume  $V$  without invoking a spherical filter function. For protohaloes, we assume that  $V$  can be approximated by an ellipsoid whose axis lengths and orientations are derived from its inertia tensor.

Once the linear tidal field has been measured in this way, we define the Lagrangian overdensity of each protohalo as  $\delta_L = \sum_i \lambda_i$ . Both the tides and the density contrast of the protohaloes are therefore evaluated within an ellipsoidal (rather than spherical) aperture whose shape and orientation is tailored to match each individual protohalo. Relative to spherical filtering, this results in per cent-level corrections to  $\delta_L$  over the range of masses we study here.

Applying this procedure to FOF haloes with  $\geq 1000$  particles ensures that even the lowest mass haloes are, on average, resolved with at least 20 grid cells. We have explicitly verified that this is sufficient to yield robust estimates of the  $\lambda_i$ s and  $\mathbf{d}_i$ s.

Note that the tidal field can be alternatively characterized in terms of its ellipticity,  $e$ , and prolateness,  $p$ . These are defined

$$e = \frac{\lambda_1 - \lambda_3}{2 \delta_L} \quad (7)$$

and

$$p = \frac{\lambda_1 - 2 \lambda_2 + \lambda_3}{2 \delta_L}. \quad (8)$$

## 4 RESULTS

### 4.1 Ellipsoidal collapse and density thresholds for CDM halo formation

Given estimates of the tidal field acting upon a given protohalo, we can use the EC model described in Section 2 to *predict* the linear density contrast required for collapse to occur at  $z_{\text{id}} = 0$ . We will discriminate “predicted” and “measured” values of  $\delta_L$  using superscripts:  $\delta_L^{\text{Sim}}$ , for example, refers to its value measured in the initial conditions of our simulations;  $\delta_L^{\text{Mod}}$  to the model-predicted value. Protohalo overdensities predicted by the EC model are shown in Figure 1, and are compared directly with the linear overdensities  $\delta_L^{\text{Sim}}$  obtained by the method described above. We



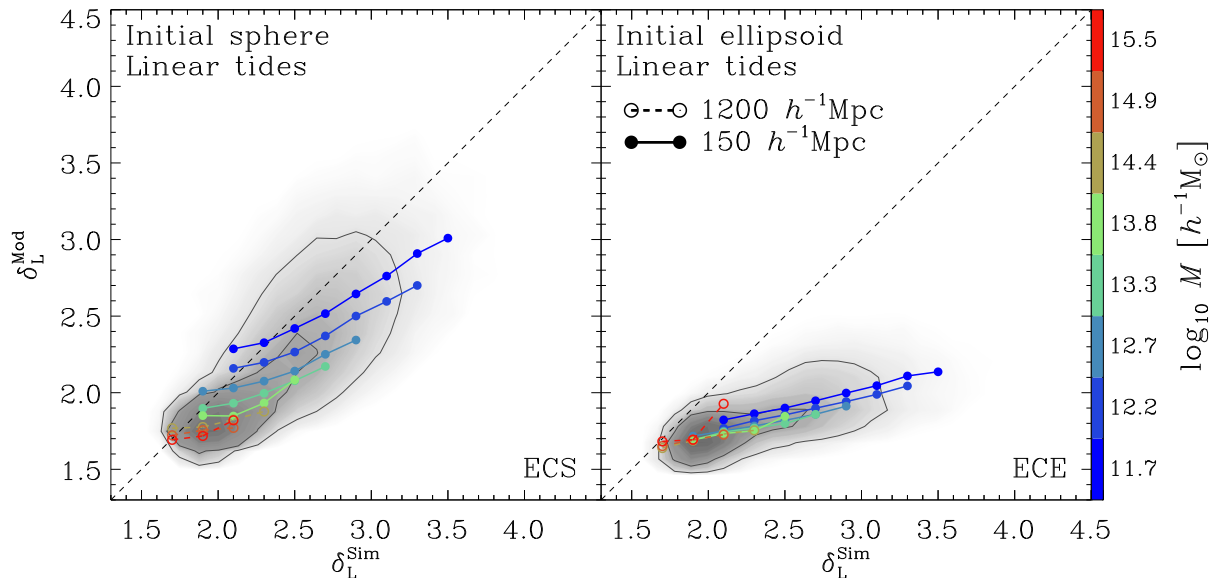


**Figure 1.** Lagrangian overdensities of dark-matter protohaloes predicted by the ellipsoidal collapse model plotted versus their overdensities measured in the initial conditions of our simulations. Model predictions assume that the Lagrangian tidal field measured at each protohalo’s center evolves according to linear theory. The left-hand panel corresponds to the EC model of BM96, ECS, which assumes that each protohalo’s initial shape can be approximated by a sphere; the right-hand panel explicitly accounts for each protohalo’s initially non-spherical shape, which we measure in the simulation initial conditions. Shaded regions highlight the density of points in the  $\delta - \delta$  plane; contours enclose 50 per cent and 80 per cent of the data. Connected points show the median values of  $\delta_L^{\text{Mod}}$  at fixed  $\delta_L^{\text{Sim}}$  measured in separate mass bins (shown using different colored lines), equally spaced in  $\log M$ . Solid circles are used for haloes in our  $150 h^{-1}$  Mpc box; open squares for those in the  $1200 h^{-1}$  Mpc box

will use these “ $\delta - \delta$ ” relations as a diagnostic for the ability of the EC model to describe the dynamics of individual dark-matter haloes.

In Figure 1 we plot, for each protohalo, the linear density contrast for collapse at  $z = 0$  predicted by the EC model versus their measured overdensities. The left hand panel shows the predictions of the EC model of BM96, which assumes that each protohalo occupies a spherical Lagrangian volume<sup>1</sup>. We will hereafter refer to this as the ECS model (for Ellipsoidal Collapse of Spherical perturbations); density contrasts predicted by this model will be denoted  $\delta_L^{\text{ECS}}$ . On the right, we have included the influence of each protohalo’s shape on the predicted collapse threshold (hereafter referred to as the ECE model, for Ellipsoidal Collapse of Ellipsoidal perturbations). Note that, in this case, the non-spherical perturbation itself contributes to the initial tidal field. We therefore modify the external component such that the total tidal field in the model initially matches the linear tidal field measured for each protohalo in the simulation. In each panel connected symbols show the median values of  $\delta_L^{\text{Mod}}$  measured in fixed bins of  $\delta_L^{\text{Sim}}$ ; different colored lines plot the relations for equally spaced logarithmic mass bins (indicated in the legend).

Note that, in both cases, the model-predicted overdensities correlate rather well with those measured directly in the initial conditions of the simulations, albeit with considerable scatter. The median trends, however, are noticeably shallower than one would expect if the ellipsoidal model

truly captures the dynamics of halo collapse. Note also that the ECS model predicts a strong mass dependence to the median  $\delta - \delta$  relations. This results from the fact that the collapse barrier (at fixed  $p$ ) depends entirely on the ellipticity of the tidal field  $e$ , growing monotonically with increasing  $e$ . Because, for random points,  $e$  scales with mass as  $e = (\sigma(M)/\delta)/\sqrt{5}$  (Doroshkevich 1970), the ECS model predicts systematically higher collapse thresholds for lower mass haloes, resulting in a segregation of the average  $\delta_L^{\text{Mod}}$ s predicted for haloes of different mass.

Intriguingly, the mass dependence disappears when individual protohalo shapes are included in the model prediction. This is because toward lower masses, protohaloes become increasingly triaxial, which lowers the density threshold required for collapse to occur in spite of the increasing tidal field strength (see Paper I). None the less, both models fail to reproduce the measured distribution of protohalo overdensities, and it is worthwhile exploring what aspects or assumptions of the EC model may result in the discrepancy.

## 4.2 The influence of external tides

One common assumption of the EC model – and indeed our assumption in constructing Figure 1 – is that the external tidal field, assumed to be generated by structure on very large scales, remains linear at all times. All ingredients needed to solve eq. (1) are therefore already present in the linear density field. In reality, a growing dark-matter halo may be subjected to interactions with nearby neighbours which may result in strongly non-linear tidal forces that act to suppress its growth and alter its collapse time

<sup>1</sup> Note that an equivalent plot was provided in Figure 3 of Sheth, Mo & Tormen (2001).

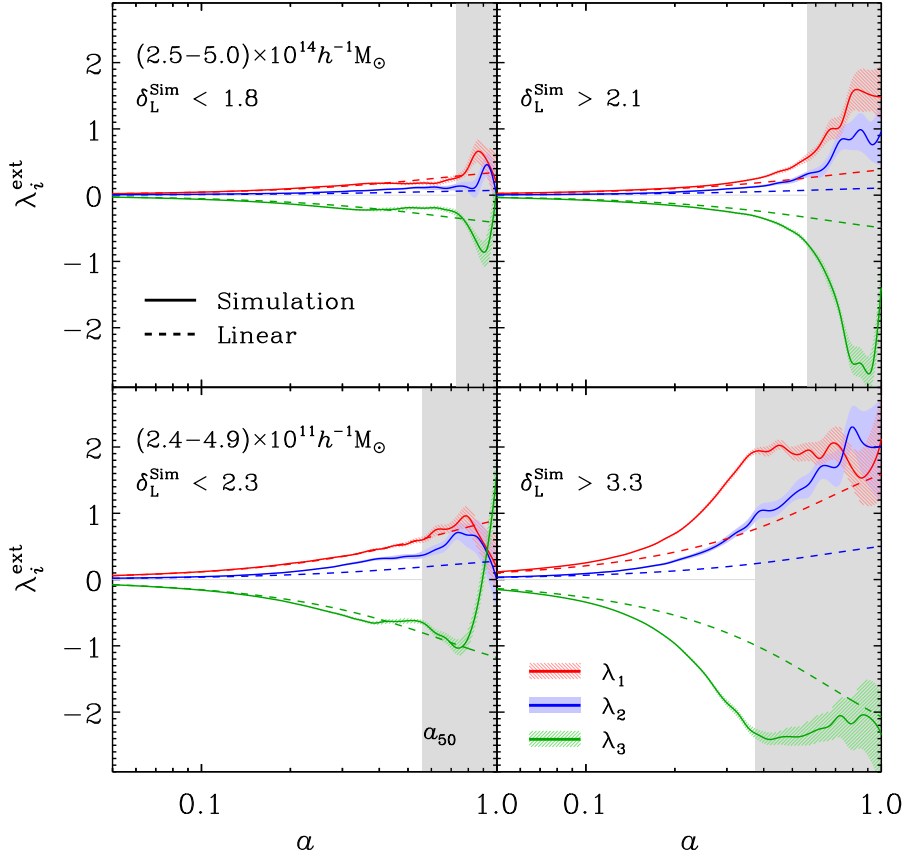


**Figure 2.** Evolution of the median external tidal field (solid lines) for haloes in two separate mass bins. Upper panels correspond to haloes in the mass range  $2.5 < M_{\text{FOF}}/(10^{14} h^{-1} M_{\odot}) < 5$ , lower panels to those with  $2.4 < M_{\text{FOF}}/(10^{11} h^{-1} M_{\odot}) < 4.9$ . Left- and right-hand panels split haloes in each mass bin according to their initial density contrast,  $\delta_{\text{L}}^{\text{Sim}}$ : those of the left include haloes that rank in the lowest 15 per cent of the  $\delta_{\text{L}}^{\text{Sim}}$  distribution, and those on the right only those in the highest 15 per cent. In each case, hatched regions correspond to the 90 per cent confidence interval on the median  $\lambda_i^{\text{ext}}(z)$  obtained by bootstrapping. For comparison, we also show the linear evolution of the median Lagrangian tidal fields measured at each halo center using dashed lines. Grey shaded regions correspond to redshifts  $z < z_{50}$ , where  $z_{50}$  is the median half-mass formation redshift of each halo sample.

(Hahn et al. 2009; Wang et al. 2011). It is therefore important to assess whether the assumption of linearly evolving tides remains valid during the evolution of simulated haloes, in order to make a more meaningful comparison between their measured and predicted overdensities.

To do so, we trace all particles belonging to each protohalo through each simulation output, and use eq. (4) to characterize the redshift dependence of the shape and orientation of each collapsing region. We approximate the geometry of this region as an ellipsoid and fix its volume,  $V$ , such that it encloses the protohalo mass at all subsequent times. The total tidal field acting upon the collapsing region is then estimated using the procedure outlined in Section 3.3. This method has two distinct advantages over using the particles themselves to define  $V$ : 1) it ensures that we follow a region with constant enclosed mass, even though the individual particles within it may change with time; 2) it allows for a simple decomposition of the total tidal field into its internal and external components.

We apply this procedure to each  $z_{\text{id}} = 0$  FOF halo (containing at least 1000 particles) and in all simulation outputs in order to explicitly measure the time evolution of

the tidal field,  $\lambda_i^{\text{tot}}(z)$ , acting upon each halo. The shape of the ellipsoid can be used to approximate the contribution of internal tides,  $\beta_i \delta / 2$ , using eq. (2) and (3), in order to estimate  $\lambda_i^{\text{ext}}(z)$ . Note that calculating the internal tides this way assumes a homogeneous density inside the ellipsoid, which may be inaccurate at late times.

The evolution of the external tidal field calculated in this way is shown in Figure 2 for haloes in two separate mass bins. Upper panels correspond to haloes that fall in the mass range  $2.5 < M_{\text{FOF}}/(10^{14} h^{-1} M_{\odot}) < 5$ ; the lower to those with  $2.4 < M_{\text{FOF}}/(10^{11} h^{-1} M_{\odot}) < 4.9$ . Panels on the left show haloes in each mass bin that rank in the lowest 15 per cent of  $\delta_{\text{L}}^{\text{Sim}}$ , whereas those on the right rank in the highest 15 per cent. (The threshold values of  $\delta_{\text{L}}^{\text{Sim}}$  are provided in each panel.) Grey shaded regions indicate redshifts below the median half-mass formation redshift for each sample, after which the assumption of a homogeneous density inside the ellipsoid is likely inaccurate. The measured  $\lambda_i^{\text{ext}}(z)$ s are shown using solid lines, as indicated in the legend, while the dashed lines show the linear extrapolation of the average Lagrangian tides measured for each halo sample.

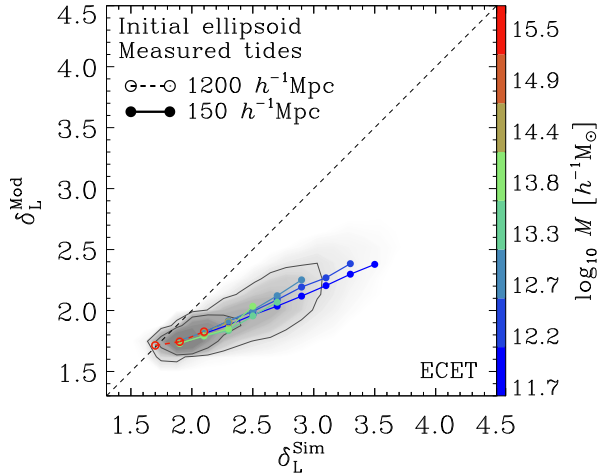


**Figure 3.** Linear density contrast predicted by the ECET model plotted against the measured Lagrangian overdensities of dark-matter protohaloes. The ECET model explicitly accounts for the non-spherical shape of each individual protohalo as well as the evolution of their external tidal fields, without resorting to the common assumption of linearly evolving tides. As in Figure 1, shaded regions indicate the density of haloes in the  $\delta - \delta$  plane; contours enclose 50 per cent and 80 per cent of the data points. Connected points show the median values of  $\delta_L^{\text{Sim}}$  at fixed  $\delta_L^{\text{Mod}}$  measured in separate mass bins, as indicated in the legend.

Massive haloes tend to evolve in environments where the tidal field scales approximately as expected from linear theory. This is not surprising given that these haloes dominate their environments and the external tides are therefore generated by long-range modes that have not yet collapsed. The same is true for low-mass haloes in low-density regions. Protohaloes with low values of  $\delta_L^{\text{Sim}}$  tend to be less clustered than those of higher  $\delta_L^{\text{Sim}}$ , with the latter forming in regions where tidal fields clearly grow more strongly than expected from a simple linear extrapolation of the Lagrangian values.

What implications do these non-linear tides have for the collapse thresholds of dark-matter haloes inferred from the EC model? Having calculated the evolution of the tidal field explicitly for each individual halo, we can insert it directly into eq. (1) in order to assess the impact of non-linear tides on the collapse thresholds inferred from the ellipsoidal collapse model. The resulting  $\delta - \delta$  relation for the ECE model is shown in Figure 3 (hereafter the ECET model) where, again, the connected points highlight medians in logarithmic mass bins.

As expected, massive haloes, and those with  $\delta_L^{\text{Sim}} \approx \delta_{\text{sc}}$ , are largely unaffected by the inclusion of explicitly measured external tides. Those with higher  $\delta_L^{\text{Sim}}$ , however, live in more clustered environments and are affected by tides that clearly evolve non-linearly. These tides act to inhibit the collapse of the density perturbations, increasing the initial density contrast required for collapse to occur at  $z = 0$ . The effect, however, is weak. For example, haloes in the lower right panel of Figure 2 are subject to external tides that deviate from the linear theory extrapolation by roughly a factor of  $\sim 2.2$  at the halo’s half-mass formation time (shaded regions indicate redshifts below the median value of  $z_{50}$  for all haloes

in each sample). This effect delays full collapse (in the ECE case) by roughly  $1.4 h^{-1} \text{Myr}$ , or, equivalently, requires an enhancement of only 12 per cent in the initial density contrast for collapse at  $z = 0$ . This is clearly not sufficient to bring the predictions of the ECE model into agreement with the simulation data, suggesting that other factors may be at play. We turn our attention to these next.

### 4.3 Collapse times

There is a clear mismatch between the predictions of the EC model and the true properties of dark-matter protohaloes when applied on a object-by-object basis. As discussed in Paper I, these differences may be related to the details of each halo’s unique evolutionary history. For example, in the EC or SC model, collapse occurring at redshift  $z_c > z_{\text{id}}$  requires an initial density contrast a factor of  $D(z_{\text{id}})/D(z_c)$  larger than what would be needed for collapse at  $z_{\text{id}}$  under the same environmental conditions. Because, at a given mass scale, haloes with higher  $\delta_L$  typically form earlier than those of lower  $\delta_L$  (Paper I), correcting the model predictions for  $z_c > 0$  may explain the discrepancy between the measured overdensities of protohaloes and the model-predicted values.

As discussed in Paper I, simple estimates of halo formation times based on the growth of their most massive progenitors fail to account for the scatter in their linear overdensities. However, unlike our simulated haloes, which grow through a sequence of mergers and smooth accretion, perturbations in the EC model remain homogeneous throughout their evolution and the collapse redshift is therefore unambiguously defined as the time at which the last axis reaches the radius  $r_{f,i} = f q_i a$ . Once collapse has occurred, the model assumes that the volume of the ellipsoid remains constant thereafter. Is there an analogous definition of “collapse” that can be easily applied to cosmological haloes?

For a dark-matter halo identified at  $z_{\text{id}} = 0$ , one can approximate the evolution of its outermost mass shell by tracking the volume  $V(a)$  of the same best-fitting ellipsoid used to calculate the external tidal field (described in Section 4.2). Its size can be used to provide a simple and intuitive estimate of the time at which its *entire*  $z = 0$  mass had first assembled into a single, dispersion-supported non-linear system.

In the upper panel of Figure 4 we plot the evolution of the volume of three such ellipsoids after averaging over subsamples of haloes in the mass range  $(2.4-2.9) \times 10^{11} h^{-1} M_{\odot}$ . The solid (black) curve shows the evolution of the median  $V(a)$  computed for all haloes in the quoted mass bin; dashed (red) and dot-dashed (blue) lines show the corresponding result for haloes that rank in the maximum and minimum 15 per cent of  $\delta_L^{\text{Sim}}$ , respectively.

On average, the present-day mass of these haloes was already in place at  $z \approx 0.7$ . More extreme examples can be found in the sample with the highest initial density contrasts, whose present-day masses reached a stable volume at  $z \approx 2$ , when the Universe was only  $\sim 15$  per cent of its current age. Attempting to predict the collapse dynamics of these haloes with models tuned for collapse at  $z = 0$  is therefore prone to systematic errors. On the other hand, haloes with the lowest value of  $\delta_L^{\text{Sim}}$  appear to have accreted their outer-most mass shells only very recently. This implies that,

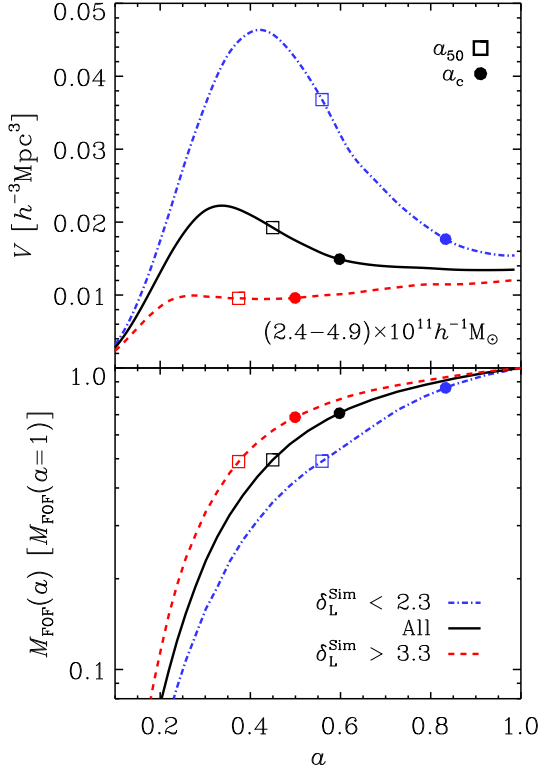


**Figure 4.** *Upper panel:* Evolution of the median volume of the ellipsoid, centered on each collapsing protohalo, that, at any  $z$ , encloses the final mass of the descendant halo at  $z = 0$  (see Section 4.3 for details). All haloes are selected to lie in a narrow mass bin, as indicated in the legend. The black solid line corresponds to the median  $V(a)$  for all haloes in that mass bin. Dashed (red) and dot-dashed (blue) lines show the evolution for the subsamples of haloes that lie in the upper-most and lower-most 15 percent of  $\delta_L^{\text{Sim}}$ . *Lower panel:* Evolution of the median FOF mass of the most massive progenitor for the same samples of haloes. In both panels, solid circles highlight the “collapse redshift”,  $z_c$ , defined in Section 4.3, whereas open squares indicate the half-mass formation time,  $z_{50}$ , at which each halo’s main progenitor first assembled half of its present-day mass.

on average, haloes with  $\delta_L^{\text{Sim}} > \delta_L^{\text{ECE}}$  have  $z_c > 0$ : strictly speaking, *these haloes collapsed before they were identified*.

This may seem to conflict with the mass accretion histories of the same haloes, shown in the bottom panel of Figure 4. These curves trace the median evolution of the FOF mass of each halo’s main progenitor, and suggest that halo masses increase at all redshifts. However, as already noted by Diemand, Kuhlen & Madau (2007), this “pseudo-growth” results from the fact that halo boundaries are defined, at any time, relative to a fixed (or slowly varying) overdensity threshold. The decrease in the cosmic background density with time therefore results in an artificial increase of halo boundaries, and hence masses (see also, Cuesta et al. 2008; Diemer, More & Kravtsov 2013; Zemp 2013). Halo finders based on fixed *physical* densities may therefore result in more realistic estimates of their masses and sizes.

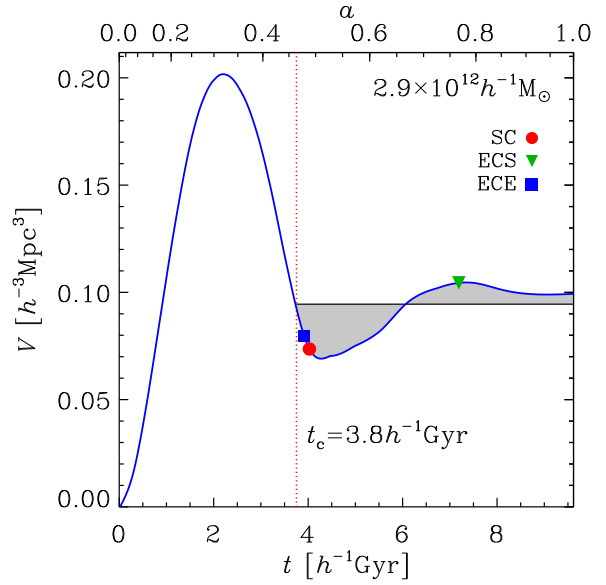


**Figure 5.** Evolution of the volume of an ellipsoid centered on the progenitor of a ( $z = 0$ )  $2.8 \times 10^{12} h^{-1} M_{\odot}$  halo that, at each redshift, encloses the present day halo mass. The shape and orientation of the best-fitting ellipsoid is explicitly calculated using the full set of particles that, at  $z = 0$ , belong to the FOF group. The evolution of the volume,  $V(z)$ , is used to estimate the “collapse redshift” of the halo,  $z_c = 1.2$  (dotted-dashed vertical line), using the condition specified in eq. (9). This definition of  $z_c$  estimates the time at which the entire  $z = 0$  halo mass had first assembled into a stable configuration, and accounts for oscillations in the volume that occur during the system’s approach toward equilibrium. The colored symbols plotted along the blue line highlight the collapse times predicted by the different versions of the EC model discussed in this paper.

None the less, we can use the trajectories of  $V(a)$  to estimate an appropriate “freezing” or collapse time,  $z_c$ , for each individual halo. This estimate of  $z_c$  can then be used to halt collapse in the EC model in order to make a more appropriate comparison between the model’s predictions and measured Lagrangian overdensities of dark-matter protohaloes.

We define  $z_c$  as earliest redshift at which the following condition is satisfied:

$$\int_{t_c}^{t_{\text{max}}} [V(t) - V(t_c)] dt = 0, \quad (9)$$

where  $t_c$  and  $t_{\text{max}}$  are the cosmological times corresponding to the collapse redshift,  $z_c$ , and the end of the simulation,  $z_{\text{max}}$ . In Figure 5 we provide an example of the evolution of  $V(a)$  (solid blue curve) for a single halo of ( $z = 0$ ) mass  $M_{\text{FOF}} \sim 2.9 \times 10^{12} h^{-1} M_{\odot}$ . The evolution mimics the expectations of simple collapse models: after an initial phase of expansion the system turns around, begins collapsing and eventually reaches a stable quasi-equilibrium configuration. The first “dip” after turnaround corresponds to a state of maximal compression in which the halo’s entire  $z = 0$  mass is briefly confined within a compact volume smaller than the present-day virial volume of the halo. This is followed by a phase of expansion, and a second (very slight) phase of contraction as the system moves toward equilibrium. These “dips” and “peaks” clearly occur *after* collapse, but before



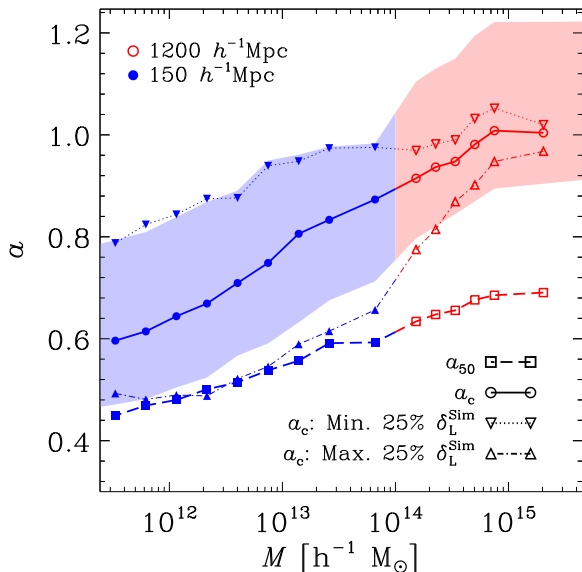


**Figure 6.** Mass dependence of halo collapse and formation times. Circles connected by solid lines show the median “collapse redshift”,  $z_c$  (defined in eq. (9)); squares connected by dashed lines show the median half-mass formation time,  $z_{50}$ , at which each halo’s main progenitor had first assembled half of its present-day mass. Triangles connected by dotted and dot-dashed lines show the median values of  $z_c$  for haloes that rank in the highest and lowest quartile of  $\delta_L^{\text{Sim}}$ . Filled and open symbols are used to distinguish haloes identified in our  $150 h^{-1}$  Mpc box from those in the  $1200 h^{-1}$  Mpc box, respectively. Shaded regions (shown only for  $z_c$ ) indicate the 25th and 75th percentiles of the scatter.

virialization. Our definition of  $z_c$  allows for these oscillations as the system relaxes to a state of equilibrium. The grey shaded region in Figure 5 highlights the integrand of eq. (9). Note that areas above and below the horizontal line cancel so that the integral vanishes. The corresponding collapse time,  $z_c \approx 1.2$ , is indicated with a vertical (red) dotted line.

In Figure 6 we plot the mass dependence of  $a_c = (1 + z_c)^{-1}$  for all  $z_{\text{id}} = 0$  haloes in each simulation. Note that we have verified that our estimates of  $z_c$  are insensitive to the snapshot output sequence by skipping even-numbered outputs and repeating the analysis. Connected, filled (blue) circles show the median trend for all haloes in our  $150 h^{-1}$  Mpc box; open (red) circles correspond to haloes in our  $1200 h^{-1}$  Mpc box. Shaded regions in each case indicate the 25th and 75th percentiles of the scatter<sup>2</sup>. As expected, the most massive haloes (those above a few  $\times 10^{14} h^{-1} M_\odot$ ) have typical collapse times of  $z_c \approx 0$ , whereas  $z_c > 0$  for lower mass haloes. The median mass dependence to  $a_c$  can be approximated by a simple linear function:

$$a_c = c_1 \log_{10}(M/[h^{-1}M_\odot]) + c_0. \quad (10)$$

<sup>2</sup> Because many massive haloes at  $z = 0$  are expected to be in a state of rapid growth, the use of eq. (9) to estimate  $z_c$  may not be justified. In order to obtain a reasonable estimate of the collapse times of massive systems we decided to extend our  $1200 h^{-1}$  Mpc box run to  $z = -0.27$ , which allowed us to track the collapse phase of even the most massive haloes identified at  $z_{\text{id}} = 0$ .

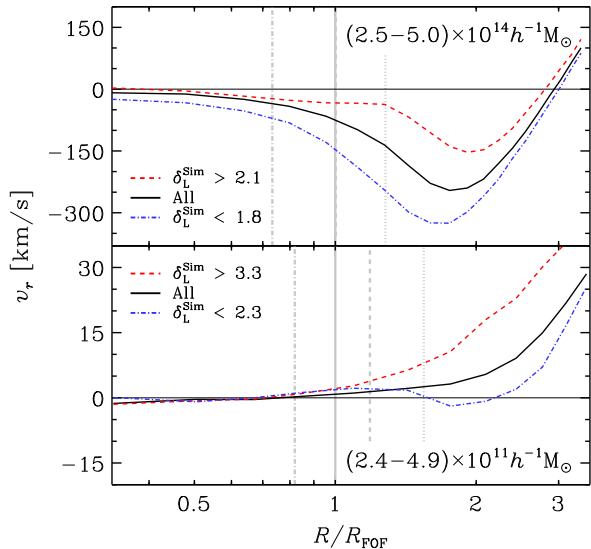


**Figure 7.** Solid black lines show the median radial velocity profiles of FOF haloes at  $z_{\text{id}} = 0$  in two separate mass bins. Dashed (red) and dot-dashed (blue) lines show the median  $v_r(r)$  for haloes that rank in the highest and lowest 15 per cent of  $\delta_L^{\text{Sim}}$ . In all cases, the radial coordinate is expressed in units of the mean size of the FOF haloes. Vertical grey lines indicate the typical size of the haloes when identified with the SO-algorithm, using an overdensity threshold of  $\Delta = 100$  (dotted), 200 (dashed) and 500 (dot-dashed), respectively. Note the different scale of the velocity axis in the upper and lower panels.

The values of the best-fitting parameters are provided in Table 1 for several different halo definitions.

#### 4.4 The collapse threshold at collapse redshift $z_c$

Adopting separate collapse and identification redshifts has a subtle implication for comparing the predictions of the EC model to the outcome of simulations. FOF haloes defined at  $z_{\text{id}} = 0$  are bounded by mass (and resolution) dependent isodensity contours. Our definition of  $z_c$ , however, defines the time at which the entire  $z = 0$  mass was first confined within approximately the same *physical* volume. As a result, the (comoving) overdensity of the halo at  $z_c$  will be lower than its  $z = 0$  value by a factor of  $(1 + z_c)^3$ . To account for the different density contrast at collapse we multiply the radial freezing factor,  $f$ , used in the EC model by  $(1 + z_c)$ .

Additional corrections to  $f$  can be made in order to account for the mass-dependence of FOF halo overdensities. For example, we find that haloes in our  $150 h^{-1}$  Mpc box have, on average,  $\Delta \approx 325$ , whereas  $\Delta \approx 270$  for those in our  $1200 h^{-1}$  Mpc run (see More et al. 2011, for a more detailed discussion of the overdensities of FOF groups). Since  $f = 0.178$  sets the  $z = 0$  virial overdensity in the spherical collapse model, we modify the radial freezing factors in the EC model to match the mean overdensities of haloes in each of our simulations. This results in  $f = 0.145$  for haloes in our  $150 h^{-1}$  Mpc box, and  $f = 0.155$  for those in the  $1200 h^{-1}$  Mpc box.

Based on the results presented in Figure 6, the vast majority of dark-matter haloes (apart from the most mas-

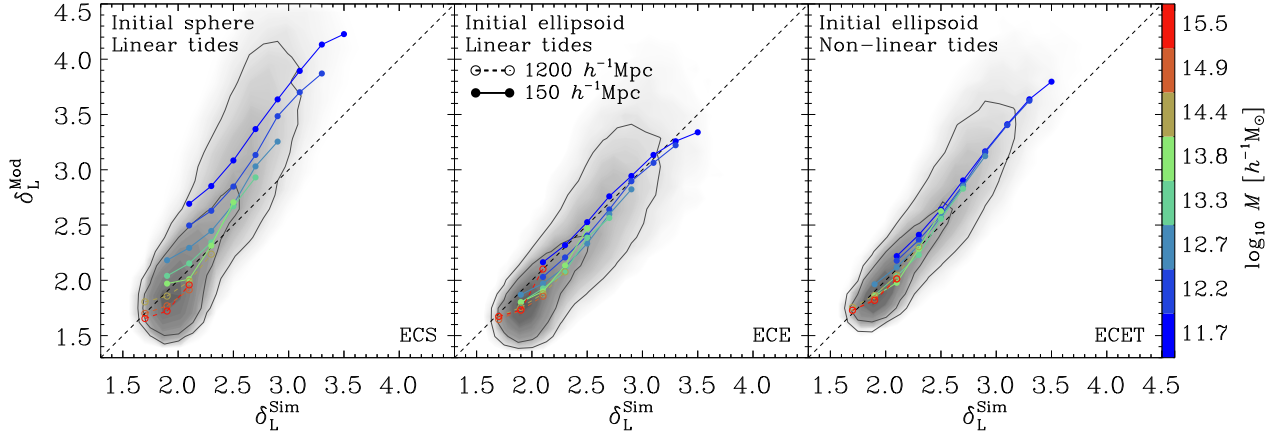


**Figure 8.** Predicted linear overdensities of dark-matter protohaloes calculated from the EC model plotted versus their measured overdensities. Predicted overdensities are calculated for collapse at  $z_c > 0$  ( $z_c$  is the collapse redshift defined by eq. (9), and is explicitly calculated for each individual halo). The left-hand panel corresponds to the predictions of the BM96, ECS model, which assumes that each protohalo occupies a spherical Lagrangian volume, and that external tidal forces evolve from their initial values according to linear theory. Predictions in the middle panel explicitly account for the non-spherical shapes of dark-matter protohaloes, as measured in the initial conditions of our simulations, but retains the linear evolution of their tidal fields (this model is referred to in the text as the ECE model). Finally, the right-most panel shows the predictions of the EC model after fully accounting for the triaxial shapes of dark-matter protohaloes, as well as the evolution of their non-linear external tidal fields (referred to as ECET). As in similar figures, the connected symbols show, for various mass bins, the median values of  $\delta_L^{\text{Mod}}$  in bins of  $\delta_L^{\text{Sim}}$ .

**Table 1.** Values obtained from fitting eq. (10) to the median collapse redshift as a function of halo mass.

Halo	$c_1$	$c_0$
FOF	0.13	-0.88
SO ( $\Delta = 100$ )	0.13	-0.81
SO ( $\Delta = 200$ )	0.12	-0.79
SO ( $\Delta = 500$ )	0.11	-0.66

sive ones) are expected to have reached stable configurations at  $z_c \gtrsim 0$ . This implies that most haloes, at the moment they are identified, are experiencing little, if any, net mass accretion. We examine this point further in Figure 7, where we plot the average radial-velocity profiles measured in spherical bins surrounding each  $z_{\text{id}} = 0$  dark-matter halo. Note that the radial coordinates have been scaled to the characteristic radius  $R_{\text{FOF}} = (3V_{\text{FOF}}(z=0)/4\pi)^{1/3}$ ; median values of the radii enclosing fixed overdensities of  $\Delta = 100, 200$ , and  $500$  are also shown as solid, dashed and dot-dashed vertical lines, respectively. Panels correspond to two separate mass bins:  $(2.5 - 5.0) \times 10^{14} h^{-1} M_\odot$  (top) and  $(2.4 - 4.9) \times 10^{11} h^{-1} M_\odot$  (bottom). Within each mass bin separate curves show the median  $v_r(r)$  profiles for all haloes (solid curve) as well as for the upper and lower-most 15 per cent of the  $\delta_L^{\text{Sim}}$  distribution.

Independent of their initial overdensity, the majority of massive haloes exhibit a strong pattern of infall in the regions surrounding the halo. The radius at which infall becomes substantial, however, is a function of  $\delta_L$  (and hence,  $z_c$ ). This suggests, that these systems are still accreting, and have not yet reached their final quasi-equilibrium state. Lower-mass haloes, on the other hand, display very little infall and are therefore not accreting mass (see also Prada et al. 2006).

The physics that determines the collapse redshift of a particular halo, or the moment at which infall is suppressed, is not well understood. None the less, practical estimates of  $z_c$ , such as that defined by eq. (9), can be used to rescale the collapse redshifts in the EC model in order to make a more meaningful prediction of the density threshold required for the perturbation to collapse. We plot the predicted density contrast for collapse at  $z_c$ , linearly extrapolated to  $z_{\text{id}} = 0$ , versus the measured protohalo overdensities (also linearly extrapolated to  $z = 0$ ) in Figure 8. For completeness, we include the results for all variants of the ellipsoidal model that we have considered, and show the median trends in the same halo-mass bins as before. In all cases, correcting for  $z_c > 0$  significantly improves the correlation between the predicted a measured protohalo overdensities.

Note that the mass dependence of the  $\delta - \delta$  relation predicted by the ECS model (seen already in Figure 1) remains after correcting for  $z_c$ . This is a result of the fact that  $z_c$  increases with decreasing mass, and therefore corrects the predicted overdensities of low-mass haloes more than those of massive ones. Haloes of  $\sim 10^{12} h^{-1} M_\odot$ , for example, have  $\langle z_c \rangle \sim 0.58$ , rather than  $z_c = 0$ . Within the ECS model, this shift in collapse time is achieved by enhancing the linear density contrast of the perturbation by roughly 35 per cent. Massive haloes ( $\gtrsim 10^{14} h^{-1} M_\odot$ ), on the other hand, have  $z_c \sim 0$  and therefore remain unchanged in this  $\delta - \delta$  plot.

Note also that the overdensities predicted by the ECE and ECET models now follow closely the one-to-one line (shown in each panel as a dashed line), with the median trend differing by, at most, 10 per cent for all halo masses and the full range of linear overdensities. The median relations for these models are also independent of halo mass: all individual lines in the middle and right-hand panels of Figure 8 neatly overlap. The fit of a linear function,  $\delta_L^{\text{Mod}} = A\delta_L^{\text{Sim}} + B$ , to individual points in the  $\delta - \delta$  plane

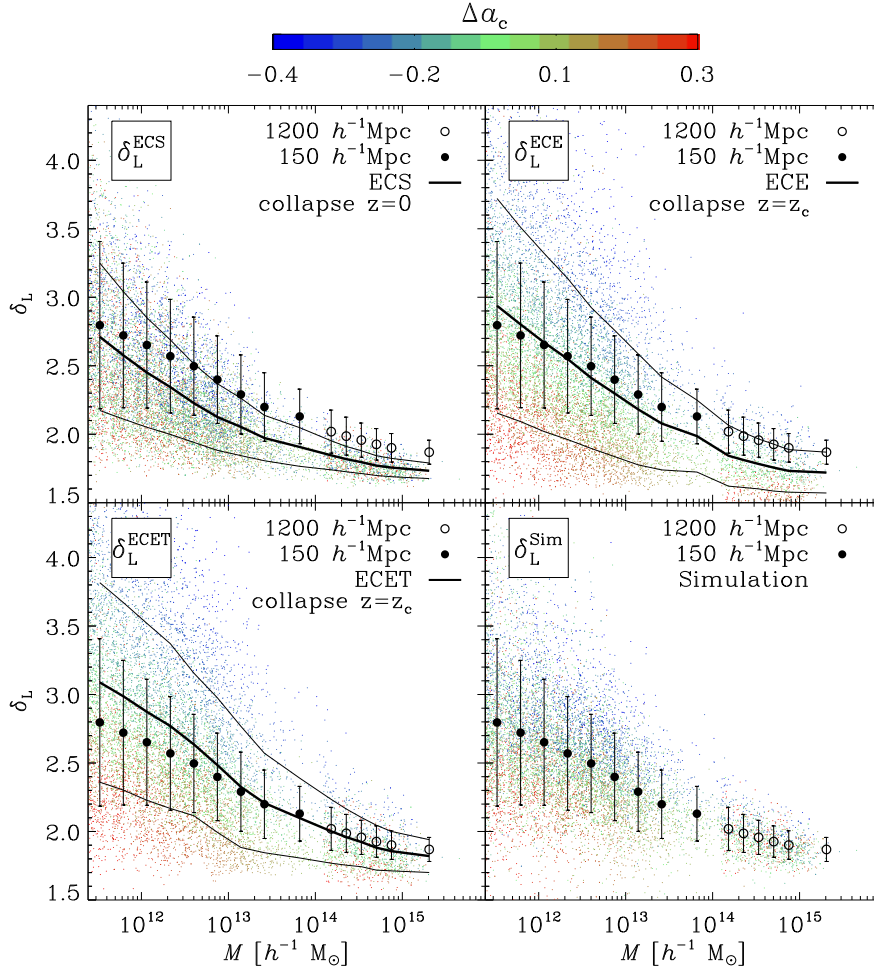


**Figure 9.** Linear density contrast as a function of mass. Points show the predicted value of the ECS model in the upper left panel, the ECE model including collapse times in the right upper panel and the ECET model including collapse times in the lower left panel. The lower right panel shows the values measured directly in the simulation. The points are colored according to  $\Delta a_c$ , the offset between the expansion factor at collapse and the corresponding mean value for haloes of the same mass (note that this color coding is different from what is used in Figure 1 of Paper I). Heavy points with error bars show the mean and standard deviation of the *measured* density contrast in bins of mass. Heavy lines show the mean of the predicted density contrast in each panel, while thin lines indicate the standard deviation. For clarity, we have randomly down-sampled points in mass bins with  $\gtrsim 1000$  haloes.

reveals that the ECE model is consistent with a one-to-one line, while the ECS model is not.

The correction to the slope of the  $\delta - \delta$  relation results from the fact that, at any given mass scale,  $\delta_L^{\text{Sim}}$  and  $z_c$  are strongly correlated. The dotted and dot-dashed lines in Figure 6 make this point clear. These curves highlight the median mass-dependence of  $z_c$  for haloes that, in each mass bin, rank in the highest and lowest 25 per cent of  $\delta_L^{\text{Sim}}$ . Clearly haloes that are initially denser tend to collapse earlier, resulting in a larger correction to their model-predicted overdensities.

## 5 DISCUSSION

### 5.1 The mass dependence and scatter of $\delta_L$

The dependence of  $z_c$  on  $\delta_L$  can also be seen in the lower-right panel of Figure 9. Here we plot the mass-dependence of

$\delta_L$  for all haloes in both of our simulations, and color points by  $\Delta a_c$ , defined by the offset between each halos collapse time,  $a_c$ , and the median value for haloes of the same mass. The mean trends are shown using solid and open points for haloes in our  $150 h^{-1}\text{Mpc}$  box and our  $1200 h^{-1}\text{Mpc}$  box, respectively; the error bars indicate standard deviation.

For comparison, we also plot the *predicted*  $\delta_L(M)$  relations in the other three panels, adopting the same color-coding for each. Data in the upper-left panel show the mass-dependence of protohalo overdensities predicted by the ellipsoidal model of BM96, tuned for  $z = 0$ ; the upper-right and lower-left panels correspond to the ECE and ECET-model predictions (both tuned for collapse at  $z_c$ ). In all cases, the mean trends at fixed mass are shown using thick solid lines, with thinner lines indicating the standard deviation at fixed  $M$ . These trends can be compared to the points with error bars, which reproduce the measured  $\delta_L(M)$  relation plotted in the lower-right panel.

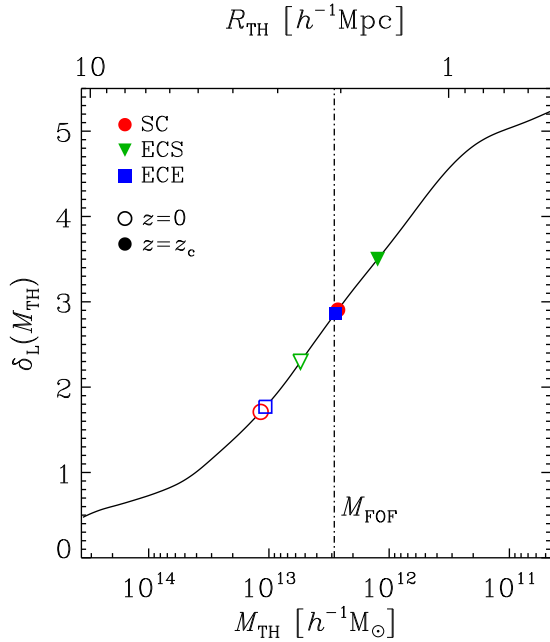


**Figure 10.** Excursion-set trajectory associated with the protohalo shown in Fig. 5.  $\delta_L(M_{\text{TH}})$  is the linear density contrast extrapolated to  $z = 0$  after averaging within a sphere of radius  $R_{\text{TH}}$  (corresponding to the mass scale  $M_{\text{TH}} = 4\pi\rho_{\text{crit}}\Omega_M R_{\text{TH}}^3/3$ ) extending around the protohalo center of mass. Open symbols highlight the points at which the trajectory crosses the threshold for collapse at  $z = z_{\text{id}} = 0$  evaluated using different collapse models. In all cases, the EPS theory substantially overestimates the halo mass measured in the simulation at  $z_{\text{id}}$  (indicated by the vertical dot-dashed line). On the other hand, when the SC and ECE models are tuned for collapse at  $z_c$  (solid symbols), the predicted halo masses are in excellent agreement with the numerical results.

Note that, while the standard ECS model systematically under-predicts the linear collapse threshold, the ECE and ECET models fare much better. Both models reproduce the mass and collapse time-dependence of  $\delta_L$  rather well; the average trends deviate by at most  $\sim 10$  per cent over roughly five orders of magnitude in mass. This is remarkable given the simplicity of the ellipsoidal model, which overlooks entirely the complex hierarchical growth of dark-matter haloes. Note also that these models predict a scatter in  $\delta_L$  that decreases with increasing mass, which is qualitatively consistent with the variance of measured protohalo overdensities. However, all models typically over-predict the scatter in  $\delta_L$  at a given mass, and it is unclear whether different estimates of halo collapse times will perform better in this regard.

## 5.2 Implications for the extended Press-Schechter formalism

Our results raise questions concerning the validity of the extended Press-Schechter (EPS) formalism (Bond et al. 1991), particularly for low-mass haloes identified at late times (i.e. those with  $\sigma(M) \gg \delta_c$ ). In the EPS theory, the outer boundary of a protohalo coincides with the initial location of a spherical mass shell that should collapse at  $z_{\text{id}}$ . However, our results demonstrate that most haloes stop accreting matter

at  $z_c > z_{\text{id}}$  and are essentially immutable thereafter. For redshifts  $z < z_c$ , the use of halo finding algorithms based on density contrasts results in the (small) pseudo-growth of the halo mass due to the decreasing background density.

We present an illustrative (and typical) example in Figure 10, where we plot the excursion-set trajectory at the Lagrangian location of the same halo used in Figure 5. The solid line shows the linear density contrast (extrapolated to  $z = 0$ ) smoothed with a spherical top-hat filter of radius  $R_{\text{TH}}$  and mass  $M_{\text{TH}}$ . The open symbols indicate the points where the trajectory crosses the threshold for collapse at  $z = z_{\text{id}} = 0$  computed using the SC (circle), ECS (triangle) and ECE (square) models. In all cases, the EPS model substantially overestimates the halo mass measured in the simulation at  $z_{\text{id}}$  (dot-dashed line). This is because, contrary to the model assumption, no mass shells were accreted onto the halo after  $z_c = 1.2$ . On the other hand, the EPS predictions are rather accurate at  $z_c$  (cf. the solid symbols and the dot-dashed line), when the ECE (or SC) model is adopted to predict the collapse threshold. This can also be seen in Fig. 5, where the same symbols mark the collapse times predicted by the different models.

We therefore disagree with the interpretation given by Sheth, Mo & Tormen (2001) that the mass dependence of the halo formation threshold  $\delta_c$  is due to the fact that denser linear perturbations are necessary to overcome stronger tides in order to guarantee collapse at  $z_{\text{id}}$ . Rather, we attribute the mass scaling to the fact that, on average, low-mass haloes collapse and stop accreting at higher redshifts than haloes of higher mass. Future work will focus on understanding the physical mechanisms that prevent the collapse of the outer material shells. Non-linear tidal interactions (e.g. Hahn et al. 2009) and the geometrical overlap of the outer Lagrangian boundaries of neighbouring haloes (Paper I) likely play a key role.

Finally, we note that the phenomenon known as “assembly bias” (see e.g. Gao, Springel & White 2005) simply reflects the dependence of the collapse threshold on  $z_c$  at fixed halo mass and identification redshift: “old” haloes ( $z_c \gg z_{\text{id}}$ ) are more biased tracers of the underlying matter distribution than “young” haloes ( $z_c \simeq z_{\text{id}}$ ).

## 6 SUMMARY

We used two high-resolution simulations of structure formation in the  $\Lambda$ CDM cosmology to test how well the EC model describes the linear density contrasts in regions that collapse to form haloes identified at  $z_{\text{id}} = 0$ . Our analysis focused on EC models of increasing complexity. The first (ECS) assumes that each protohalo can be approximated by a spherical Lagrangian tophat perturbation acted upon by linearly evolving external tidal forces, as described in BM96. The second model (ECE) allows for initially non-spherical perturbations, but retains the linear evolution of external tides (this model was described in detail in Paper I). Finally, we consider a model (ECET) which accounts for both the non-spherical initial shape of protohaloes, as well as the fact that their external tidal fields evolve non-linearly. Our main results can be summarized as follows.

(i) The ECS model fails to describe the linear density contrasts measured at the sites of halo collapse in the initial



conditions of our simulations. In this model, the required density contrast for collapse (at fixed  $z_c$ ) is determined entirely by the surrounding tidal field, i.e. by  $e$  and  $p$ . Because the average tidal field strength decreases with mass, the ECS prediction is strongly mass-dependent, and is unable to reproduce the measured density contrasts of haloes on an object-by-object basis, as evident in Figure 1. For example, protohaloes with the same linear density contrast, but with final masses of  $10^{12}$  and  $10^{14} h^{-1} M_\odot$ , have predicted  $\delta_L^{\text{ECS}}$  values that differ systematically by  $\sim 30$  per cent.

(ii) The mass dependence of the predicted protohalo overdensity disappears completely when their measured initial shapes are properly accounted for in the model calculation. This is because initially triaxial perturbations that align with the eigenvectors of their external tidal field typically collapse at lower overdensities than their spherical brethren when acted upon by strong external tides (Paper I). The mass dependence of protohalo shapes (in which lower mass haloes are systematically less spherical) therefore balances the higher initial density contrasts needed for low-mass systems to overcome the strong tidal forces in the ECS model. Nevertheless, when tuned for collapse at  $z = 0$ , the model still fails to predict the observed range of Lagrangian overdensities measured in our simulations, succeeding only for very massive haloes and those with low initial density contrasts.

(iii) In order to better understand these results, we developed an accurate method to measure the time evolution of the strength and orientation of the external tidal field acting upon a collapsing halo. This method reproduces the linear evolution of external tides for massive haloes, and for those forming in low density regions, but shows a clear non-linear evolution for highly clustered haloes in the initial density field. Although non-linear tides act to inhibit the collapse of dense protohaloes (and therefore increase the model-predicted density contrasts for collapse at  $z = 0$ ), incorporating these effects into the EC model only slightly improves the agreement between the model prediction and the measured Lagrangian overdensities of protohaloes.

(iv) The main discrepancy between the predicted and measured protohalo overdensities can be accurately accounted for if one drops the assumption that haloes are collapsing *today*. For a given tidal ellipticity,  $e$ , and prolativity,  $p$ , the barrier height for collapse at redshift  $z_c > z_{\text{id}}$  predicted by the EC model is larger by factor of  $D(z_{\text{id}})/D(z_c) > 1$ . We devised a simple method of calculating  $z_c$ : it does not depend on halo merger histories or on the growth of the main progenitor, but approximately estimates the earliest time at which the entire  $z = 0$  mass of the halo first reached a stable volume. Using this, we showed that a modified EC model that accounts for both the triaxial nature of protohaloes as well as the collapse times of their descendants, can predict the Lagrangian density contrast of protohaloes in an unbiased way.

(v) Although the ECE and ECET models provide a more faithful description of the density thresholds required for gravitational collapse, they rely heavily on input from the simulations. This substantially reduces the predictability of these models, but illuminates possible avenues for future progress. For example, a deeper understanding of the connection between the overdensities of protohaloes and their collapse times,  $z_c$ , would undoubtedly result in a much more

powerful analytic model for halo formation. This would have important implications for theoretical modeling of, among other things, large-scale structure, the halo mass function, and the merger trees of dark matter halos.

Our results suggest that the Lagrangian overdensity of regions that collapse to form haloes by  $z = 0$  increase toward lower halo masses (see also Robertson et al. 2009; Elia, Ludlow & Porciani 2012). Within the context of the standard model for ellipsoidal collapse (referred to here as the ECS model) this behavior results from the fact that lower-mass haloes are subject to stronger tidal distortion and therefore require larger initial overdensities to collapse by a particular time (Sheth, Mo & Tormen 2001). Our results suggest a different interpretation. One difference results from the much weaker dependence of  $\delta_{\text{ec}}$  on external tides when protohaloes are modeled as triaxial ellipsoids rather than spheres. This substantially reduces the model-predicted density threshold required for the collapse of low-mass (or strongly sheared) perturbations by  $z = 0$ . On the other hand, the vast majority of low-mass haloes had already assembled their total  $z = 0$  masses at  $z_c > 0$ , suggesting that model barriers tuned for collapse *today* are underestimating the true barrier height. In this interpretation, the shape of the  $\delta_L(M)$  relation simply reflects the mass-dependence of halo collapse times: low-mass haloes collapse, on average, earlier than more massive ones, and therefore have higher initial density contrasts. This interpretation is supported by the fact that, at fixed halo mass,  $\delta_L$  depends strongly on  $z_c$  but not on the shape or strength of the surrounding tidal field.

## ACKNOWLEDGMENTS

MB acknowledges financial support from from the Deutsche Forschungsgemeinschaft through the Transregio 33, “The Dark Universe”, and ADL through the SFB (956), “The Conditions and Impact of Star Formation”. We wish to thank our referee, Aseem Paranjape, for a constructive report that has improved this paper.

## REFERENCES

- Angrick C., Bartelmann M., 2010, A&A, 518, A38+
- Bardeen J. M., Bond J. R., Kaiser N., Szalay A. S., 1986, ApJ, 304, 15
- Bertschinger E., Jain B., 1994, ApJ, 431, 486
- Bond J. R., Cole S., Efstathiou G., Kaiser N., 1991, ApJ, 379, 440
- Bond J. R., Myers S. T., 1996, ApJS, 103, 1
- Cuesta A. J., Prada F., Klypin A., Moles M., 2008, MNRAS, 389, 385
- Del Popolo A., 2002, A&A, 387, 759
- Despali G., Tormen G., Sheth R. K., 2013, MNRAS, 431, 1143
- Diemand J., Kuhlen M., Madau P., 2007, ApJ, 667, 859
- Diemer B., More S., Kravtsov A. V., 2013, ApJ, 766, 25
- Doroshkevich A. G., 1970, Astrofizika, 6, 581
- Efstathiou G., Frenk C. S., White S. D. M., Davis M., 1988, MNRAS, 235, 715
- Eisenstein D. J., Loeb A., 1995, ApJ, 439, 520

- Eke V. R., Cole S., Frenk C. S., 1996, *MNRAS*, 282, 263  
 Elia A., Ludlow A. D., Porciani C., 2012, *MNRAS*, 421, 3472  
 Gao L., Springel V., White S. D. M., 2005, *MNRAS*, 363, L66  
 Gott, III J. R., Rees M. J., 1975, *A&A*, 45, 365  
 Gunn J. E., Gott, III J. R., 1972, *ApJ*, 176, 1  
 Hahn O., Paranjape A., 2014, *MNRAS*, 438, 878  
 Hahn O., Porciani C., Dekel A., Carollo C. M., 2009, *MNRAS*, 398, 1742  
 Hockney R. W., Eastwood J. W., 1988, *Computer simulation using particles*. Adam Hilger, Bristol and Philadelphia  
 Hoffman Y., 1986, *ApJ*, 308, 493  
 Icke V., 1973, *A&A*, 27, 1  
 Kaiser N., 1984, *ApJ*, 284, L9  
 Komatsu E. et al., 2009, *ApJS*, 180, 330  
 Lahav O., Lilje P. B., Primack J. R., Rees M. J., 1991, *MNRAS*, 251, 128  
 Lee J., Pen U., 2000, *ApJ*, 532, L5  
 Lin C. C., Mestel L., Shu F. H., 1965, *ApJ*, 142, 1431  
 Ludlow A. D., Borzyszkowski M., Porciani C., 2014, *MNRAS*, 445, 4110  
 Lynden-Bell D., 1964, *ApJ*, 139, 1195  
 More S., Kravtsov A. V., Dalal N., Gottlöber S., 2011, *ApJS*, 195, 4  
 Partridge R. B., Peebles P. J. E., 1967, *ApJ*, 147, 868  
 Peebles P. J. E., 1967, *ApJ*, 147, 859  
 Peebles P. J. E., 1980, *The large-scale structure of the universe*, Peebles, P. J. E., ed.  
 Pillepich A., Porciani C., Hahn O., 2010, *MNRAS*, 402, 191  
 Porciani C., Dekel A., Hoffman Y., 2002, *MNRAS*, 332, 339  
 Prada F., Klypin A. A., Simonneau E., Betancort-Rijo J., Patiri S., Gottlöber S., Sanchez-Conde M. A., 2006, *ApJ*, 645, 1001  
 Press W. H., Schechter P., 1974, *ApJ*, 187, 425  
 Robertson B. E., Kravtsov A. V., Tinker J., Zentner A. R., 2009, *ApJ*, 696, 636  
 Sheth R. K., Mo H. J., Tormen G., 2001, *MNRAS*, 323, 1  
 Sheth R. K., Tormen G., 1999, *MNRAS*, 308, 119  
 Springel V., Yoshida N., White S. D. M., 2001, *New Astronomy*, 6, 79  
 Wang H., Mo H. J., Jing Y. P., Yang X., Wang Y., 2011, *MNRAS*, 413, 1973  
 White S. D. M., Silk J., 1979, *ApJ*, 231, 1  
 Zel'Dovich Y. B., 1970, *A&A*, 5, 84  
 Zemp M., 2013, *ArXiv e-prints*, 1312.4629

In Figure A1 we plot the resulting  $\delta-\delta$  (for collapse at  $z_c$  rather than at  $z = 0$ ). In general, we find that all conclusions drawn from our analysis of FOF haloes remains valid for SO haloes as well, suggesting that our interpretation should not be affected by halo definition.

## APPENDIX A: SO-HALO FINDER

In order to test the sensitivity of our results to our adopted (FOF) halo definition, we have repeated the analysis on dark-matter haloes identified using a spherical overdensity (SO) algorithm. Our SO halo finder identifies local maxima in the evolved density field and grows spheres around them until a given density contrast,  $\Delta$ , is reached. For this analysis we have adopted three different over-density values:  $\Delta = 100, 200$  and  $500$ . All aspects of the analysis were carried out as described in Section 3.3, including modifications to the model freezing factor,  $f$ , required to match the ( $z = 0$ ) SO-halo overdensities at  $z = 0$ .

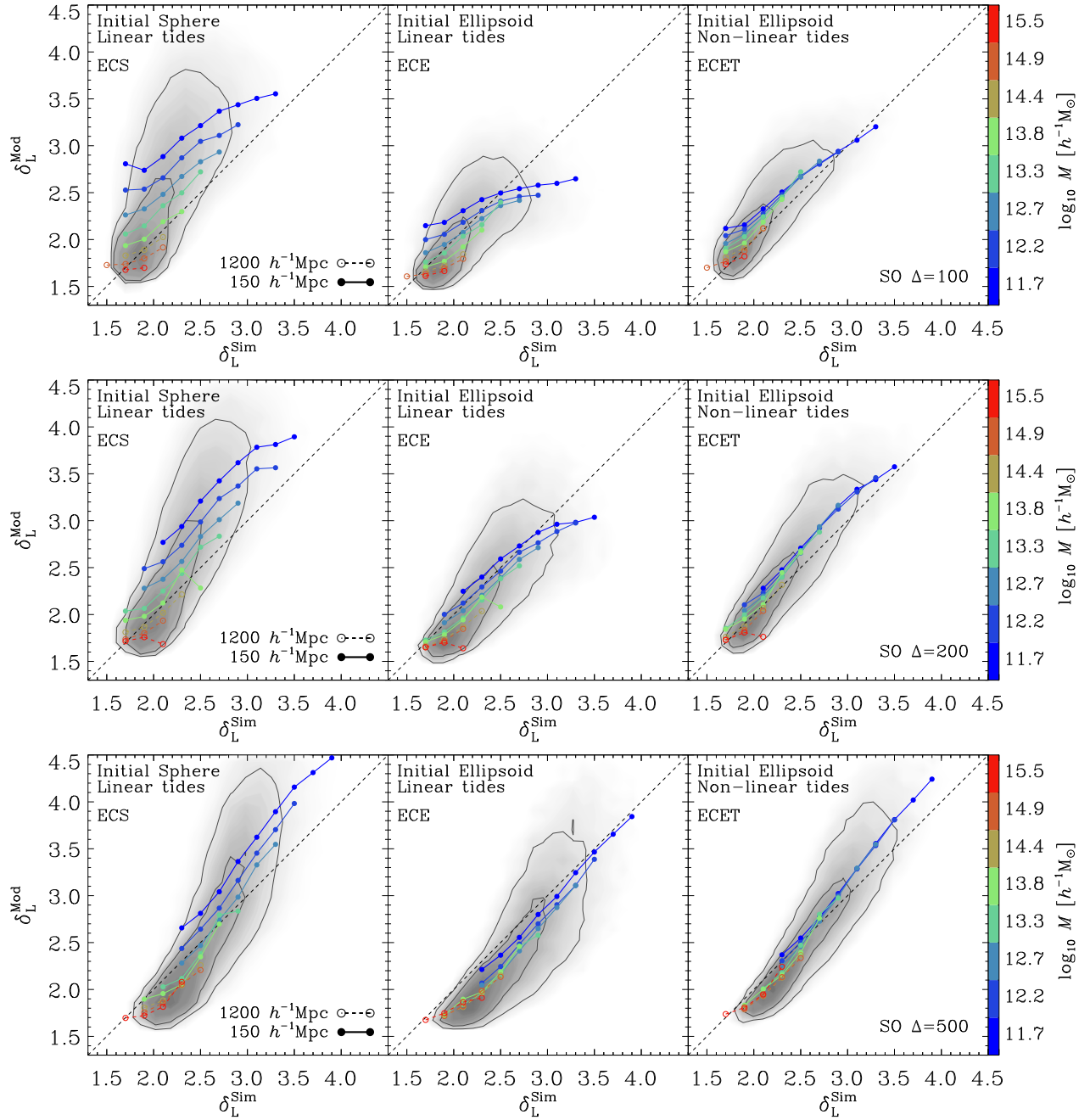


**Figure A1.** Same as Figure 8 but for haloes identified using the spherical overdensity algorithm with density contrast thresholds of 100, 200 and 500.